# Interpretation of Lorentz microscopy observations of vortices in high-temperature superconductors with columnar defects

M. Beleggia,[1,*] G. Pozzi,[1] J. Masuko,[2] N. Osakabe,[2,3] K. Harada,[3,4,5] T. Yoshida,[3,5] O. Kamimura,[3,5,†] H. Kasai,[3,4,5] T. Matsuda,[3,4,5] and A. Tonomura[3,4,5]

[1]*Department of Physics and Istituto Nazionale per la Fisica della Materia, University of Bologna, Viale B. Pichat 6/2, 40127 Bologna, Italy*

[2]*Department of Physics, Tokyo Institute of Technology, Ohokayama, Meguro-ku, Tokyo 152-8551, Japan*

[3]*Advanced Research Laboratory, Hitachi Ltd., Hatoyama, Saitama 350-0395, Japan*

[4]*Frontier Research System, The Institute of Physical and Chemical Research (RIKEN), Wako, Saitama 351-0198, Japan*

[5]*SORST, Japan Science and Technology Corporation (JST), 3-4-15 Nihonbashi, Chuo-ku, Tokyo 103-0027, Japan*

(Received 18 July 2002; published 22 November 2002)

In order to interpret recent experimental observations of superconducting vortices interacting with tilted columnar defects in high-temperature superconducting materials, we have extended to the case of anisotropic materials our Fourier space approach for the calculation of the electron optical phase shift experienced by the high-energy electrons in a transmission electron microscope. The case of a London vortex having its core not perpendicular to the specimen surfaces is considered. The same configuration is also analyzed in the framework of a simplified pancake model and the influence of the number of stacks on the phase shift and images is investigated. The results obtained by the two models are compared between them and with the experimental results. The agreement between theory and experiment confirms that anisotropy plays a major role in affecting the electron microscopy images.

DOI: 10.1103/PhysRevB.66.174518 PACS number(s): 74.60.Ge, 68.37.Lp

## I. INTRODUCTION

Recently it has been shown that the Fourier space approach, formerly introduced to cope with vortex (or fluxon) lattices,[1] can be usefully applied for the calculation of the phase shift and corresponding phase contrast images of superconducting vortices observed by transmission electron microscopy techniques.[2] In that paper, hereafter referred to as paper I, the basic ideas of the approach were introduced and applied to the investigation of a few problems. First, the case of a London vortex having its core perpendicular to the specimen surfaces has been considered, and the analytical results obtained in the Fourier space compared with the approximated ones obtained by means of the former real space approach.[3] Then, the limiting case of a specimen whose thickness is much smaller than the London penetration depth, first introduced by Pearl,[4] has been analyzed and extended to the case of a stack of three layers,[5] a useful simple model for the interpretation of vortex images in high critical temperature, $T_c$, layered materials.

In this paper the Fourier approach is applied to models which are suggested by the latest experiments,[6] where superconducting specimens irradiated with heavy ions in a direction different from the normal have been studied in order to directly observe the pinning of the vortices at columnar defects. In particular, the first analysis of the contrast features strongly suggests that anisotropy plays an important role in determining the outcome of transmission electron microscopy experiments.[7,8]

Therefore, in order to interpret the experimental results in the most accurate and appropriate way and to properly take into account the influence of anisotropy we have investigated the model of a tilted London vortex in a thin anisotropic slab and, on the other hand, extended the pancake model calculations by increasing the number of layers. The obtained results are presented, discussed, and compared to experimental results taken in a variety of different conditions. The applied magnetic field was low enough to make sure that the vortices can be considered isolated. In fact, at higher fields and in the presence of columnar defects, the distortion of the flux line lattice and the resulting loss of periodicity make the use of Fourier methods rather troublesome.

It will be shown that the satisfying agreement between theory and experiments confirms the soundness of these models for the interpretation of the data and better clarifies the role played by anisotropy.

## II. GENERAL CONSIDERATIONS

Let us first introduce the main conventions regarding the coordinate systems and the basic formulas describing the interaction of the electron beam with the magnetic field associated with the pinned vortex, where the assumption is made that the normal core lies along the columnar defect. As the latter is tilted with respect to the surfaces, and the specimen itself can in turn be rotated around its normal in the cooling stage in order to vary the overall geometry of the experiment, we should slightly change the notation with respect to paper I in order to take into account these new experimental features.

Therefore our starting points are the same two coordinate systems introduced in paper I, namely: (i) the microscope coordinate system having the $z$ axis parallel to the electron beam and aligned in the same direction, with $(x,y)$ being the coordinates in the object plane, perpendicular to the optical axis $z$, and (ii) the specimen reference system $(x_S,y_S,z_S)$, having its $z_S$ axis, of unit vector $\mathbf{k}_S$, coincident with the

 

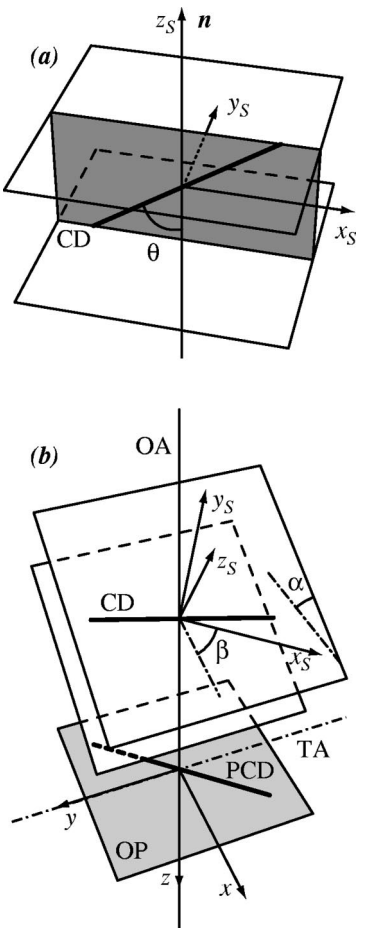


FIG. 1. Schematic view of the geometry involved: (a) specimen reference system $(x_S, y_S, z_S)$; (b) microscope reference system $(x,y,z)$. TA: tilt axis; OA: optical axis; CD: columnar defect; PCD projected columnar defect on the object plane; $\alpha$: specimen tilt angle; $\beta$: specimen azimuth rotation angle; $\theta$: columnar defect tilt angle.

specimen normal **n** and oriented in the opposite direction as $z$, the $x_S$ axis, of unit vector $\mathbf{i}_S$, having initially the same direction as $x$, and the $y_S$ axis determined by the requirement of left-handedness, i.e., opposite to $y$.

We assume that the columnar defect (CD) lies initially in the $(x_S, z_S)$ plane [shadowed in Fig. 1(a)] and forms an angle $\theta$ with the $z_S$ axis. The specimen, assumed of constant thickness $t$, is then inclined of an angle $\alpha$ with respect to the electron beam, around the tilt axis (TA), coincident with the $y$ (and $y_S$) axis, as indicated in Fig. 1(b). In addition, as mentioned, it is also rotated of an azimuth angle $\beta$ around its normal **n**, coincident with the tilted $z_S$ axis. This means that the new configuration is like the one sketched in the upper part of Fig. 1(b). Although, strictly speaking, the origin of the two systems coincides with the intersection of the optical axis (OA) with the midplane of the specimen, for clarity purposes, the object plane (OP), $(x,y)$, is displayed in Fig. 1(b) in the lower part and slightly offset. Also the projection of the columnar defect (PCD), which is rotated with respect to the $x$ axis of an angle dependent on $\alpha$ and $\beta$, is sketched.

The new relations between the unit vectors of the microscope and specimen systems are given by

$$\begin{aligned}\mathbf{i}_S &= \mathbf{i}\cos\alpha\cos\beta + \mathbf{j}\sin\beta + \mathbf{k}\sin\alpha\cos\beta,\\ \mathbf{j}_S &= \mathbf{i}\cos\alpha\sin\beta - \mathbf{j}\cos\beta + \mathbf{k}\sin\alpha\sin\beta,\\ \mathbf{k}_S &= \mathbf{i}\sin\alpha - \mathbf{k}\cos\alpha,\end{aligned} \tag{1}$$

whereas corresponding relations hold between coordinates.

In order to describe the interaction between the electron beam and the magnetic field associated with the vortex, the standard high-energy or phase object approximation is used, according to which the vortex is a pure phase object,[9] with the magnetic phase shift given by

$$\varphi(x,y) = -\frac{e}{\hbar}\int_l \mathbf{A}\cdot dl = -\frac{e}{\hbar}\int_{-\infty}^{+\infty} A_z(x,y,z)\,dz, \tag{2}$$

where $\mathbf{A}$ is the vector potential, $e$ and $\hbar$ are the absolute value of the electron charge and the reduced Planck constant, respectively, and $x$ and $y$ are kept fixed since we consider an electron trajectory parallel and in the same direction as the $z$ axis.[10]

This trajectory passes through the regions above, within, and below the specimen, thus crossing three separated space domains. For the calculation of the phase shift by means of Eq. (2), in order to avoid unwanted extra terms arising from contour integrals on the domain boundary, it is essential to choose a vector potential continuous in its components parallel to the boundaries.[2]

In the specimen system, the above trajectory is characterized by the parametric equation

$$l = (x_S - w\tan\alpha\cos\beta)\mathbf{i}_S + (y_S - w\tan\alpha\sin\beta)\mathbf{j}_S + w\mathbf{k}_S, \tag{3}$$

where $w$ ranges between $(+\infty, -\infty)$. The correspondence between the coordinates of the intersection of the trajectory with the object plane $(x,y)$ and with the specimen midplane $(x_S, y_S)$ is given by

$$x_S = x\frac{\cos\beta}{\cos\alpha} + y\sin\beta, \quad y_S = x\frac{\sin\beta}{\cos\alpha} - y\cos\beta \tag{4}$$

Therefore, the phase shift Eq. (2) can be calculated in the specimen system according to the relation

$$\varphi(x_S, y_S) = \frac{e}{\hbar}\int_{+\infty}^{-\infty} \mathbf{A}(x_S - w\tan\alpha\cos\beta, y_S - w\tan\alpha\sin\beta, w)\cdot\begin{pmatrix}\tan\alpha\cos\beta\\ \tan\alpha\sin\beta\\ -1\end{pmatrix} dw \tag{5}$$

and converted finally in the microscope reference system through the indicated coordinate transformations.

Once the object phase $\varphi(x,y)$ is calculated for a specimen tilted at an angle $\alpha$, and rotated by an azimuth angle $\beta$, it may be displayed by means of ideal amplified contour maps, where the intensity $I(x,y)$ is given by

$$I(x,y)=1+\cos[n\varphi(x,y)] \tag{6}$$

with $n$ the amplification factor.

As regards the Fresnel phase contrast method, starting from the object phase the out of focus images in the observation plane, located at a distance $Z$ from the object plane, can be calculated by means of the Kirchhoff-Fresnel integral:[11]

$$I(X,Y,Z)=\left|\frac{1}{\lambda_e Z}\int\int \exp[i\varphi(x,y)]\exp\left(\frac{i\pi}{\lambda_e Z}[(x-X)^2+(y-Y)^2]\right)dx\,dy\right|^2, \tag{7}$$

where $X$ and $Y$ are the coordinates in the out-of-focus plane, and $\lambda_e$ is the de Broglie wavelength of the incident electrons.

## III. TILTED LONDON VORTEX IN AN ANISOTROPIC THIN FILM

In this section we follow the general scheme introduced by Kogan, Simonov, and Ledvij,[12] in order to generalize the results of paper I to the case of a straight tilted London vortex in an anisotropic uniaxial thin film, having its $c$ axis perpendicular to the film surfaces, so that the anisotropy tensor $\mathcal{L}$ in the specimen coordinate system $(x_S,y_S,z_S)$ is diagonal, having elements $\lambda_{ab}^2$, $\lambda_{ab}^2$ and $\lambda_c^2$ respectively.

Whereas identical in the basic approach, our analysis differs from that of Kogan, Simonov, and Ledvij[12] because the emphasis is put on the vector potential, which is the basic quantity for the calculation of the electron optical phase shift, and not on the magnetic field.

The vector potential must satisfy in the vacuum regions above and below the specimen the Laplace equation

$$\boldsymbol{\nabla}^2\mathbf{A}=0 \tag{8}$$

and the modified London equation within the specimen

$$\mathbf{A}-\mathcal{L}\boldsymbol{\nabla}\times\boldsymbol{\nabla}\times\mathbf{A}=\phi_0\frac{\mathbf{r}_F\times\mathbf{k}_F}{r_F^2}\equiv\boldsymbol{\Phi}_L \tag{9}$$

The second member of Eq. (9) ($\boldsymbol{\Phi}_L$ is defined as the London vector) shows that the case of a London vortex with its core and its magnetic flux aligned along $\mathbf{k}_F$ is being considered; $\mathbf{r}_F$ represents a two-dimensional position vector perpendicular to the direction $\mathbf{k}_F$ of the core. Finally, $\phi_0=h/2e$ is the superconducting flux quantum.

Since the specimen can be freely rotated, and a uniaxial anisotropic material ($\lambda_a=\lambda_b=\lambda_{ab}$) is investigated, the components of $\mathbf{k}_F$ in the specimen reference system can be chosen as $(\sin\theta,0,\cos\theta)$, where $\theta$ is the angle of the core with the $z_S$-axis, without loss of generality.

The solution in the film $\mathbf{A}^{\text{int}}$ can be written as the sum of two terms:

$$\mathbf{A}^{\text{int}}=\mathbf{A}^B+\mathbf{A}^S \tag{10}$$

The first, $\mathbf{A}^B$, which is a particular solution of the inhomogeneous equation, is identical to the London solution for the anisotropic bulk superconductor. The second, $\mathbf{A}^S$, which is the general solution of the homogeneous equation, is a surface correction term necessary to satisfy the boundary conditions.

Let us analyze these problems separately by using two-dimensional Fourier methods, suggested by the presence of flat boundaries parallel to the $(x_S,y_S)$ plane,[12] according to the general expressions

$$\tilde{\mathbf{A}}(k_x,k_y,z)=\int\int dx\,dy\,\mathbf{A}(x,y,z)e^{-i(xk_x+yk_y)} \tag{11}$$

and

$$\mathbf{A}(x,y,z)=\int\int\frac{dk_x dk_y}{4\pi^2}\,\tilde{\mathbf{A}}(k_x,k_y,z)e^{i(xk_x+yk_y)}. \tag{12}$$

In this way, since both the London (for the superconductor) and the Laplace (for the external space) equations are of the second order, the remaining dependence on the third $z$ coordinate contains simple exponential functions.

In the following, as the intermediate and final expressions are very lengthy and cumbersome, we will outline only the main steps and assumptions of the derivation.

### A. The bulk vortex solution

The Fourier transform of the London vector $\tilde{\boldsymbol{\Phi}}_L$ is given in the $S$ coordinate system by

$$\tilde{\boldsymbol{\Phi}}_L(k_{x_S},k_{y_S},z_S)=\frac{i\phi_0}{k_\theta^2}\begin{pmatrix}k_{y_S}\cos^2\theta\\-k_{x_S}\\-k_{y_S}\sin\theta\cos\theta\end{pmatrix}e^{-iz_S k_{x_S}\tan\theta} \tag{13}$$

where $k_\theta^2=k_{x_S}^2+k_{y_S}^2\cos^2\theta$.

In order to evaluate the Fourier transform of the particular solution of the inhomogeneous equation $\tilde{\mathbf{A}}^B$ we can use the fact that for the infinite straight vortex in the bulk it does not depend on the longitudinal coordinate along the vortex direction $\mathbf{k}_F$, so that $\tilde{\mathbf{A}}^B$ should have the same $z_S$ dependence as the Fourier transform of the London vector.

We therefore look for a solution in the form

$$\tilde{\mathbf{A}}^B=\tilde{\mathbf{A}}^v e^{-iz_S k_{x_S}\tan\theta} \tag{14}$$

By multiplying the former expression by $e^{i(x_S k_{x_S}+y_S k_{y_S})}$ and inserting the result in the London equation, it results in an algebric system of equations for the unknown $\tilde{\mathbf{A}}^v=(A_x^v,A_y^v,A_z^v)$ which can be easily solved.

It can be ascertained that the resulting vector potential $\mathbf{A}^B$ gives the correct magnetic field associated with the bulk London vortex but it is not divergence-free. This additional, but not essential requirement, can be easily met, so that we can finally express, after some simplifications, the Fourier transform of $\mathbf{A}^B$ as

$$\tilde{\mathbf{A}}^B(k_{x_S},k_{y_S},z_S) = \frac{i\phi_0}{\Delta_1\Delta_2 k_\theta^2}\begin{pmatrix} k_{y_S}(\cos^2\theta+\lambda_c^2 k_\theta^2) \\ -k_{x_S}[1+(\lambda_c^2+\lambda_{ab}^2\tan^2\theta)k_\theta^2] \\ -\Delta_1 k_{y_S}\sin\theta\cos\theta \end{pmatrix} \times e^{-iz_S k_{x_S}\tan\theta}, \tag{15}$$

where

$$\Delta_1=1+\lambda_{ab}^2 k_{x_S}^2+\lambda_{ab}^2 k_{y_S}^2+\lambda_{ab}^2 k_{x_S}^2\tan^2\theta, \tag{16}$$

$$\Delta_2=1+\lambda_c^2 k_{x_S}^2+\lambda_c^2 k_{y_S}^2+\lambda_{ab}^2 k_{x_S}^2\tan^2\theta. \tag{17}$$

### B. The homogeneous solution

We look now for a solution of the Fourier transform of the vector potential satisfying the homogeneous London equation in the form of a linear combination of exponential functions of $z_S$:

$$\tilde{\mathbf{A}}^S(k_{x_S},k_{y_S},z_S)=\sum_n \tilde{\mathbf{A}}^{(n)}e^{\alpha_n z_S}. \tag{18}$$

By imposing the condition that each term is also solution of the homogeneous London equation, we obtain a homogeneous linear system of equations, which has nonvanishing solutions provided its determinant vanishes. It turns out that all possible values of $\alpha_n$ are given by

$$\alpha_{1,2}=\pm\left(\frac{1+\lambda_{ab}^2 k_S^2}{\lambda_{ab}^2}\right)^{1/2} \tag{19}$$

and

$$\alpha_{3,4}=\pm\left(\frac{1+\lambda_c^2 k_S^2}{\lambda_{ab}^2}\right)^{1/2} \tag{20}$$

where $k_S^2=k_{x_S}^2+k_{y_S}^2$.

Correspondingly, we have

$$\tilde{\mathbf{A}}^{(1)}=c_1\begin{pmatrix} -\dfrac{k_{y_S}}{k_{x_S}} \\ 1 \\ 0 \end{pmatrix}, \tag{21}$$

$$\tilde{\mathbf{A}}^{(2)}=c_2\begin{pmatrix} -\dfrac{k_{y_S}}{k_{x_S}} \\ 1 \\ 0 \end{pmatrix}, \tag{22}$$

$$\tilde{\mathbf{A}}^{(3)}=c_3\begin{pmatrix} \dfrac{\lambda_{ab}k_{x_S}(1+\lambda_c^2k_S^2)^{1/2}}{\lambda_c^2k_S^2} \\ \dfrac{\lambda_{ab}k_{y_S}(1+\lambda_c^2k_S^2)^{1/2}}{\lambda_c^2k_S^2} \\ 1 \end{pmatrix}, \tag{23}$$

and

$$\tilde{\mathbf{A}}^{(4)}=c_4\begin{pmatrix} -\dfrac{\lambda_{ab}k_{x_S}(1+\lambda_c^2k_S^2)^{1/2}}{\lambda_c^2k_S^2} \\ -\dfrac{\lambda_{ab}k_{y_S}(1+\lambda_c^2k_S^2)^{1/2}}{\lambda_c^2k_S^2} \\ 1 \end{pmatrix}. \tag{24}$$

The coefficients $c_i$ will be determined by the boundary conditions of the internal field with that in the vacuum.

### C. Vacuum solutions and boundary conditions

The next problem is to find the vector potential outside the sample, $\mathbf{A}^{(+)}$ in the region $z_S>t/2$ and $\mathbf{A}^{(-)}$ in the region $z_S<-t/2$. By imposing that also the condition $\nabla\cdot\mathbf{A}=0$ is satisfied and that the vector potential vanishes at $\pm\infty$, the following expressions are obtained for the two-dimensional Fourier transforms

$$\tilde{\mathbf{A}}^{(+)}=e^{-z_S k_S}\begin{pmatrix} c_5 \\ c_6 \\ i\dfrac{c_5k_{x_S}+c_6k_{y_S}}{k_S} \end{pmatrix}, \tag{25}$$

$$\tilde{\mathbf{A}}^{(-)}=e^{z_S k_S}\begin{pmatrix} c_7 \\ c_8 \\ -i\dfrac{c_7k_{x_S}+c_8k_{y_S}}{k_S} \end{pmatrix}. \tag{26}$$

So we are left with eight coefficients $c_i$ to be determined by the boundary conditions at the upper ($z_S=t/2$) and the lower ($z_S=-t/2$) surfaces: the eight necessary equations can be obtained by the continuity of the tangential components of the vector potential and of the magnetic field.

Needless to say, calculations are very cumbersome, and the use of a computer algebra system like MATHEMATICA[14] is of an invaluable help. Also in this case, however, it is convenient first to use the boundary conditions relative to the vector potential to obtain a reduced system in the unknowns

$c_1 - c_4$. The symmetry of the resulting system makes it rather easy to reduce it again into a system of two equations in the unknowns $c_1$ and $c_2$ and this last system can finally be solved to get the desired solution.

Going back, all the coefficients can be obtained and hence the complete solution for the vector potential which, although very complicated, is nonetheless analytical in the Fourier space.

The correctness of this solution and of the method of obtaining it has been tested by calculating the vector potential and the magnetic field for the case of an anisotropic superconductor filling a half-space: our solution is identical to that found by Kogan, Simonov, and Ledvij.[12] To have still more confidence, we have also reversed the procedure, starting from the solution of the magnetic field and by obtaining from it the vector potential, under the constraint $\nabla \cdot \mathbf{A} = 0$: the result differs from the previous one by the gradient of a function, meaning that both vector potentials are equivalent regarding the field and the phase shift.

### D. Phase shift

It is helpful to present maps of the phase shifts, i.e., of the projected magnetic field, experienced by a coherent electron plane wave in an ideal experiment where the beam direction is parallel to one of the coordinate system axis and the apparent infinite thickness of the specimen is overlooked.[3]

In the case of a phase map calculated along the $y_S$ axis the following expression will be employed:

$$\phi(x_S, z_S) = \frac{i}{\phi_0} \int_0^\infty \tilde{A}_y(k_{x_S}, 0, z_S) \sin(x_S k_{x_S}) dk_{x_S}, \quad (27)$$

whereas similar expressions are valid for the phase shifts calculated along the $x_S$ or $z_S$ axis.

Figure 2 shows the phase maps calculated in the three orthogonal directions $(x_S, y_S, z_S)$ for a vortex laying on the columnar defect which is tilted at an angle $\theta = 45°$ with respect to the specimen normal ($z_S$ axis). The projected view of the columnar defect is indicated by the short bold line [white in Fig. 2(c)] in the plots. The first three plots (a,b,c) correspond to an isotropic material with $\gamma = 1$ ($\gamma$ is the anisotropy parameter, defined as the ratio between $\lambda_c$ and $\lambda_{ab}$, i.e., $\gamma = \lambda_c / \lambda_{ab}$), while the last one (d) to a medium anisotropic material with $\gamma = 5$.

In the $x_S$ and $y_S$ projections, no visible difference can be appreciated between the plots corresponding to different values of $\gamma$. This is because when we calculate the phase shift in the $x_S$ or $y_S$ direction, the only significant contribution comes from the tangential components of the vector potential, which are independent of $\lambda_c$. Therefore, the isotropic and anisotropic cases are identical in this case and only one example, the isotropic case, is reported.

On the contrary, the second row reports a striking difference between the two cases examined. Each contour line represents a phase shift of 10 mrad, and when the anisotropy parameter $\gamma$ is increased, the phase shift decreases drastically, as can be seen in the last plot, Fig. 2(d). It can be ascertained that increasing furthermore the value of $\gamma$ (a realistic case can be up to 200 or more), the phase shift is on the order of some microradians, well below the detectability limit of $\pi/100 \simeq 30$ mrad.[13]

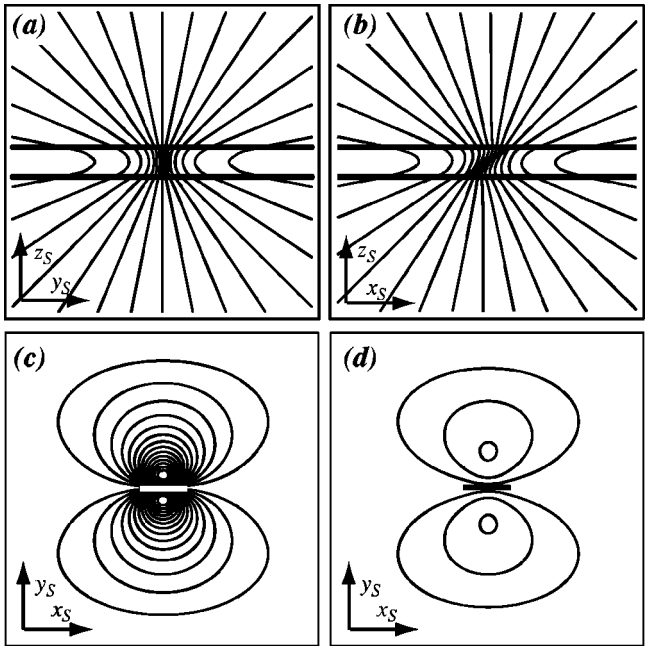


FIG. 2. Contour line plots representing the phase shift, or projected magnetic flux, in three orthogonal directions $x_S$ (a), $y_S$ (b), and $z_S$ (c),(d). (a)–(c) Isotropic case $\gamma = 1$; (d) medium anisotropy case $\gamma = 5$. The contour lines represent phase shifts of 200 mrad in (a) and (b) and of 30 mrad in (c) and (d). Simulation parameters: tilt angle $\theta = 45°$, $\lambda_{ab} = 200$ nm, plot region $4\,\mu$m.

To better clarify the situation, we have calculated the effect of an increasing anisotropy parameter $\gamma$ on the distribution of the $j_c$ current density flowing along the $z_S$ axis, and we confirmed that the main effect of a large $\lambda_c$ is a dramatic reduction of this component. While in the isotropic case the $j_c$ component is significant and comparable to $j_{ab}$, as soon as $\gamma > 1$, $j_c$ tend to decrease and, eventually, to disappear. The functional behavior of the current density is reported in Fig. 3, for three values of the anisotropy parameter $\gamma = 1,5,10$. To represent the three plots using the same vertical scale, the two curves corresponding to the anisotropic cases $\gamma = 5,10$ have been amplified by a factor $15\times$.

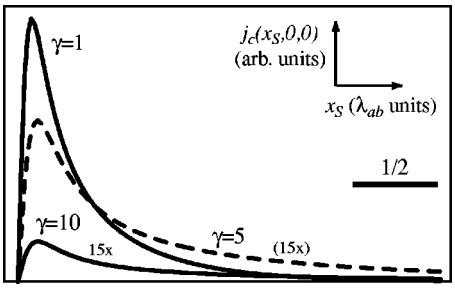


FIG. 3. Current density along the $z_S$ axis as a function of $x_S$, for the $\gamma$ values of 1,5,10. The last two cases are amplified by a factor $15\times$ in order to plot them on the same vertical scale of the isotropic plot $\gamma = 1$.

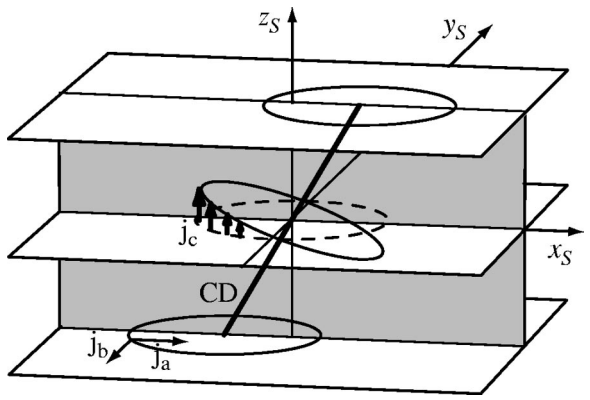


FIG. 4. Current density components at various depths. At the specimen surfaces, there is no $j_c$ (upper and lower plane circles), while inside the material $j_c$ forces the current to flow off the $ab$ plane (inner tilted circle).

Taking into account the shown results, we can try to picture the current distribution noting that when $j_c$ is absent, and only $j_a, j_b$ remain, the currents flow only in the $(x_S, y_S)$ plane. This happens at the specimen surfaces independent of the value of $\gamma$ because no current can flow toward the vacuum (to obtain a vanishing current at the surfaces is a confirmation of the correctness of the boundary condition chosen). Instead, inside the material, where $j_c$ have a nonvanishing value, the currents can flow also across the planes $z_S$=const, showing the tendency to be perpendicular to the vortex core, as visualized in Fig. 4. When, on the contrary, $j_c$ decreases and it is almost negligible also inside the material, the current flow can be considered almost confined in the $(x_S, y_S)$ plane.

This plot assumes an even greater significance when we compare it with the pancake case, as will be done in Sec. IV, because it confirms that the pancake model with no Josephson coupling is the limit of the anisotropic one for $\gamma \to \infty$. In fact, the pancake vortices are intrinsically confined in the copper-oxide planes, and $j_c$ is in this case identically zero everywhere inside the specimen.

## IV. PANCAKE VORTICES

Let us turn to the problem of extending the calculations of paper I to a stack of thin layers, which can mimic well the structure of highly anisotropic superconductors.

As stressed by Pearl[4] in a thin film, or single layer at $z_S = 0$, all quantities change over distances larger than $\lambda_{ab}$, so that they can be considered approximatively constant across the film and it is reasonable to average them over the layer thickness $t_L$.[5,12] Therefore, the problem is reduced to that of finding the field distribution in the free space, imposed by the proper boundary conditions at the film surface.

As shown in paper I, for a single layer these conditions are given by the continuity of the vector potential across the layer and by the following equation which has been obtained by averaging the modified London equation over the layer thickness:[15]

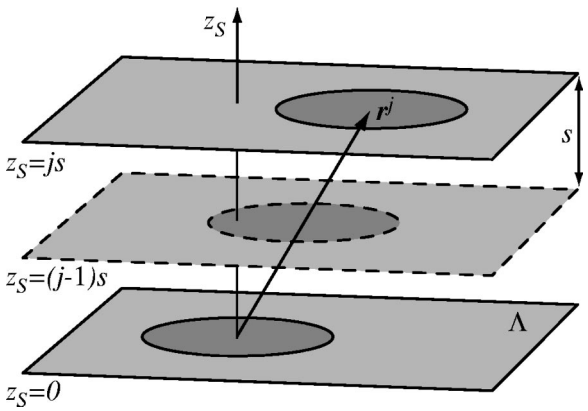


FIG. 5. Scheme of a specimen composed of $n$ layers, showing the relative position of the pancake vortex on the $j$th layer (having height $z_S = js$). Each layer is characterized by the Pearl penetration depth $\Lambda = \lambda_{ab}^2/t$, where $t=(n-1)s$.

$$\mathbf{A}(x_S, y_S, 0) - \Lambda \left\{ \left[ \frac{\partial \mathbf{A}}{\partial z_S} \right]_{0+} - \left[ \frac{\partial \mathbf{A}}{\partial z_S} \right]_{0-} \right\} = \phi_0 \frac{\mathbf{r}_S \times \mathbf{k}_S}{x_S^2 + y_S^2}, \tag{28}$$

where $\Lambda = \lambda_{ab}^2/t_L$ is the Pearl film penetration depth. This equation relates the normal derivatives at the upper ($z_S = 0^+$) and lower ($z_S = 0^-$) surfaces with the averaged vector potential. When no vortex is present and the layer is perfectly superconducting, its diamagnetic response is given by the boundary conditions above with the second member put equal to zero.

For the case of a set of $n$ layers, at coordinates $z_S^j = js$ ($s$ is the interlayer spacing), each having a London vortex at the

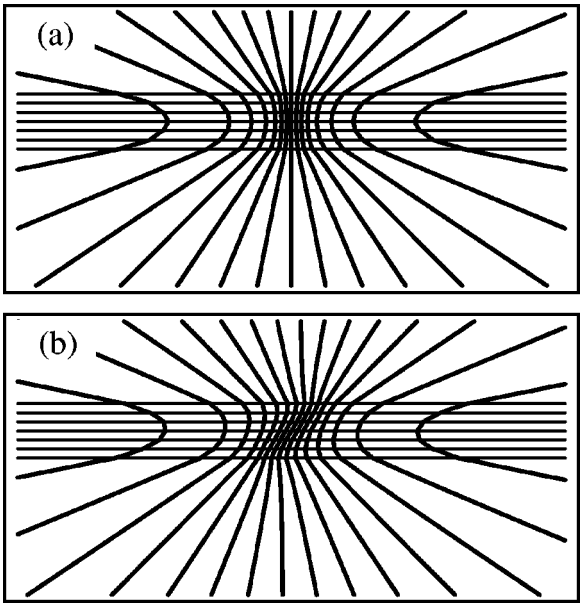


FIG. 6. Contour line plots representing the phase shift calculated with the pancake model ($n=7$ layers) in two orthogonal directions $x_S$ (a) and $y_S$ (b). The contour lines represent phase shifts of 200 mrad. Simulation parameters: tilt angle $\theta = 45°$, plot region 4 $\times 2$ $\mu$m.

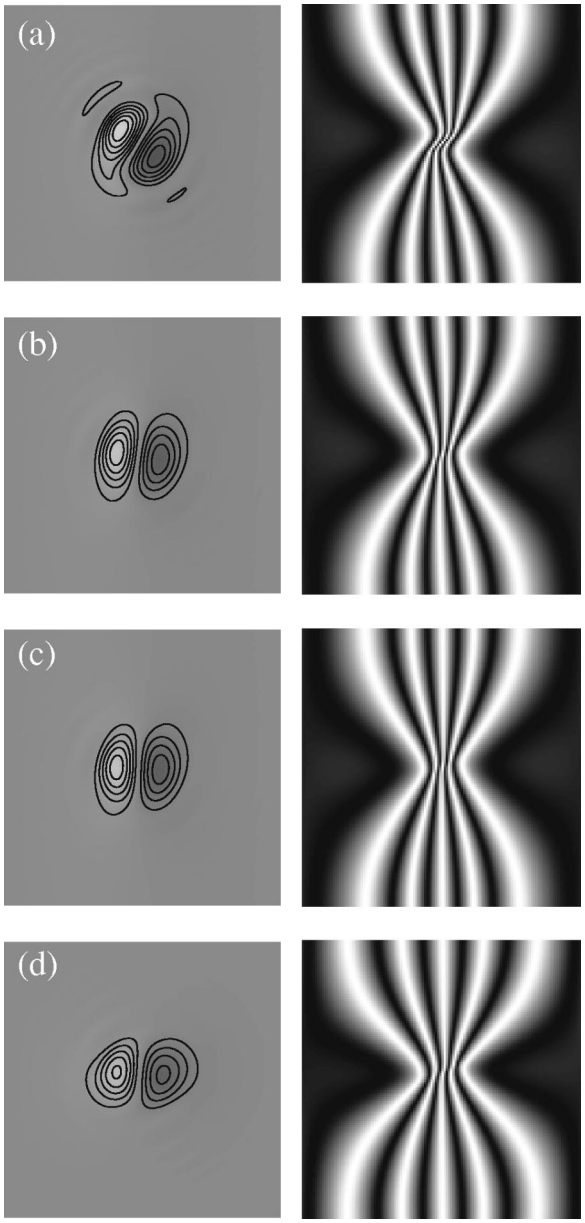


FIG. 7. Out-of-focus images (left column) and holographic contour maps 32× amplified (right column) for the following values of the anisotropic parameter: $\gamma=1,5,50,\infty$ (from top to bottom). The columnar defect tilt angle is $\theta=45°$ and the specimen rotation is $\beta=90°$.

position $\mathbf{r}^j=(x_S^j,y_S^j,z_S^j)$, the above mentioned relation can be transformed into the following one, rewritten in the two dimensional Fourier space:

$$\tilde{\mathbf{A}}(k_{x_S},k_{y_S},z_S^j)-\Lambda\left\{\left[\frac{\partial\tilde{\mathbf{A}}}{\partial z_S}\right]_{z_S^j+}-\left[\frac{\partial\tilde{\mathbf{A}}}{\partial z_S}\right]_{z_S^j-}\right\}$$
$$=\frac{i\phi_0}{k_S^2}\begin{pmatrix}k_{y_S}\\-k_{x_S}\\0\end{pmatrix}e^{-i(x_S^jk_{x_S}+y_S^jk_{y_S})}, \qquad (29)$$

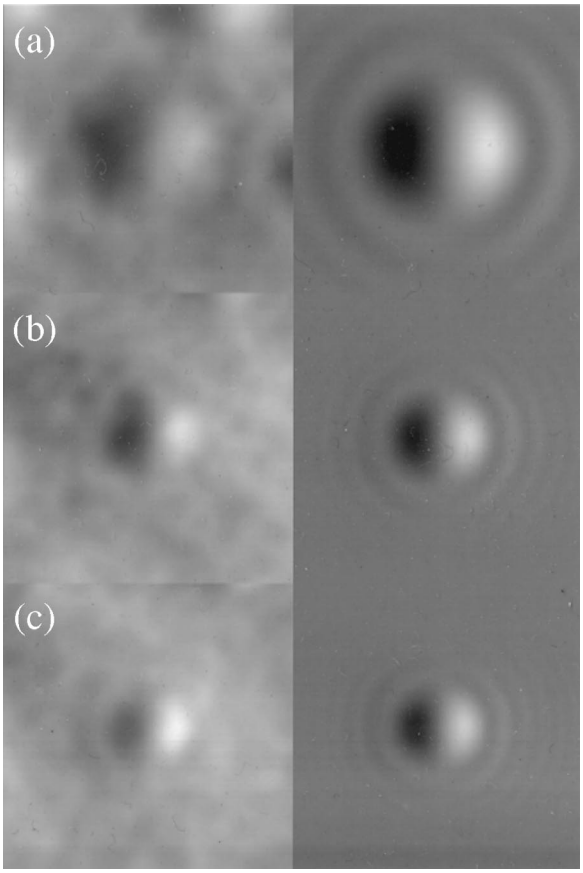


FIG. 8. Out-of-focus images, unpinned vortex (corresponding to $\theta=0°$ and an arbitrary value of $\beta$).

where $k_S^2=k_{x_S}^2+k_{y_S}^2$ and $\Lambda$ now depends on the number of layers and on the interlayer spacing $s$, according to the relation: $\Lambda=(n-1)\lambda_{ab}^2/t$. This definition follows from the total specimen thickness composed of $n-1$ interlayer spacings: $t=(n-1)s$.

In this scheme, each vacuum region between two layers will be characterized by a vector potential of the form

$$\tilde{\mathbf{A}}=\mathbf{D}^+e^{z_Sk_S}+\mathbf{D}^-e^{-z_Sk_S}, \qquad (30)$$

whereas the external regions are characterized by vector potentials like Eqs. (25) or (26), i.e., given by

$$\tilde{\mathbf{A}}^{(+)}=\tilde{\mathbf{C}}^{(+)}e^{-z_Sk_S}, \quad \tilde{\mathbf{A}}^{(-)}=\tilde{\mathbf{C}}^{(-)}e^{z_Sk_S}. \qquad (31)$$

All these coefficients can be determined by imposing the boundary condition Equation (29) and that of the continuity of the vector potential at the films, which, in the case of interest to us here, can be taken equally spaced in a stack along the $z_S$ axis, with an interlayer distance $s$ and characterized by the same Pearl penetration depth $\Lambda$. The parameters $x_S^j,y_S^j$ are obtained from the condition of considering a vortex piercing the films obliquely, being pinned at a straight columnar defect (see Fig. 5).

In order to have some idea about the trend of the field distribution, we can, as in paper I and in Sec. III D, show the phase shift calculated following Eq. (27) along the $x_S$ and $y_S$

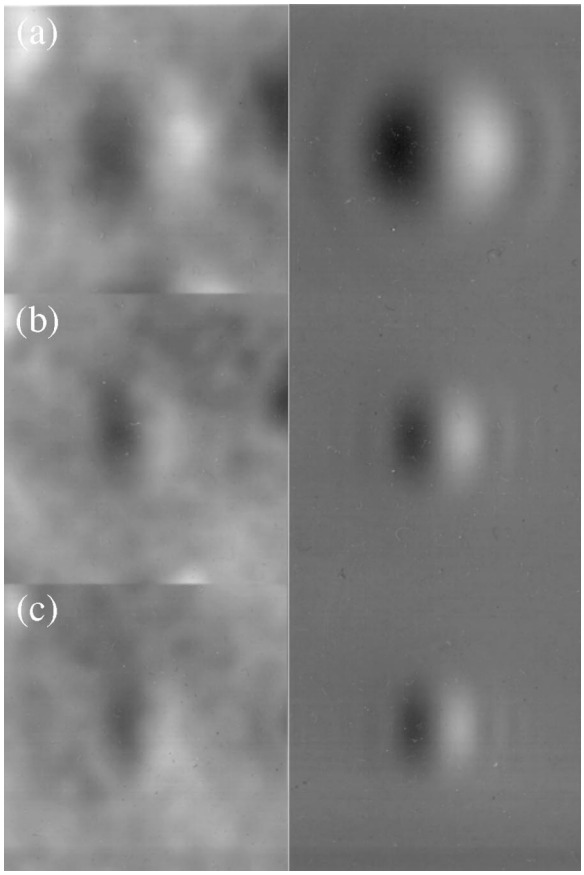


FIG. 9. Out-of-focus images, $\theta=65°, \beta=360°$.

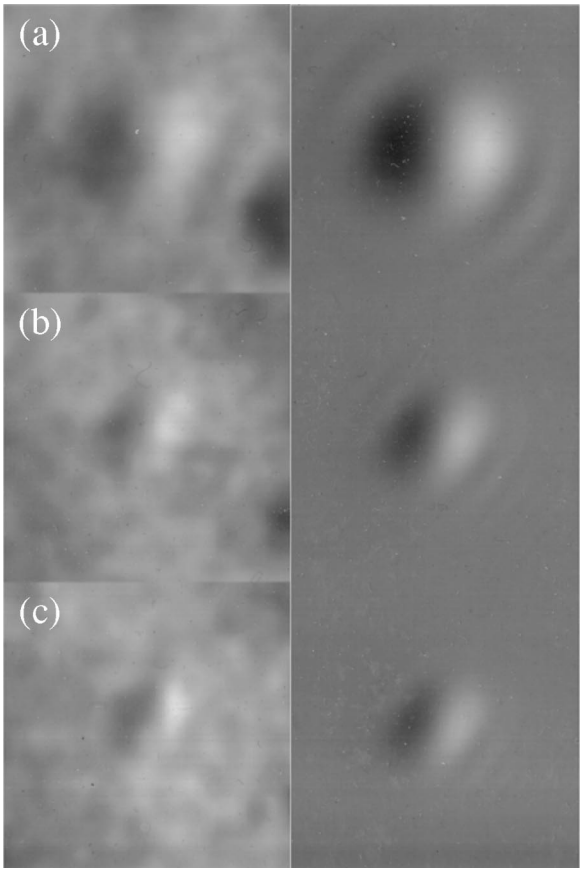


FIG. 10. Out-of-focus images, $\theta=65°, \beta=315°$.

axis. Of course, here it is not necessary to display the $z_S$-axis phase shifts similar to those reported in Figs. 2(c) and 2(d), because such a phase shift is here identically zero. In fact, the vector potential has no $A_z$ component, therefore no current density along the $z_S$ axis will flow.

Figure 6 shows the obtained result with $n=7$ layers. Once again, by means of these plots it is difficult to appreciate the difference between the isotropic case [Figs. 2(a) and 2(b)] and the pancake case reported here. However, referring to Fig. 4 it can be realized that this case corresponds to an infinite anisotropy, where the current density along the $z_S$ axis completely disappears.

## V. COMPARISON BETWEEN THE DIFFERENT MODELS

To better show how the three cases examined—isotropic, anisotropic and pancake—are indeed different, we have to resort to the calculation of phase contrast images, and finally, in Sec. VI, to compare these results with the experiment.

Figure 7 shows a series of out-of-focus and holographic images calculated for increasing $\gamma$ values, from 1 to infinity (corresponding to the pancake model). Analyzing the progressive disappearance of the apparent vortex tilt, some conclusions can be drawn: these phase contrast techniques are sensitive enough on the variation of $\gamma$ when the parameter is close to the unity, but they predict almost indistinguishable images when $\gamma>10$.[7]

The only visible difference which can be appreciated between pancake and continuous anisotropic models is a slight deformation of the contrast contour lines. In the pancake simulation (d) the globule appears less elongated, with respect to (c) which is a continuous anisotropic simulation calculated for the value $\gamma=50$. This discrepancy can be explained by the limited number of layers considered. The number $n=7$, in fact, is probably not enough to reach a correct description of the flux configuration inside the material, because the real number of layers is of the order of 200, with a real interlayer spacing of the order of the nanometer. Unfortunately, from the computational point of view, it is not yet possible to increase furthermore the number of layers. However, the contrast value (number of contrast contour lines) and the general image features are well in agreement.

The main consequence is that we cannot obtain an estimate of the anisotropic parameter itself from the analysis of the experimental images of strong anisotropic materials. Only an anisotropic superconductor characterized by $\gamma<10$, like $YBa_2Cu_3O_{7-\delta}$, $(Y-123)$ for example, could reveal the difference between the two models, for suitably chosen experimental conditions.

## VI. EXPERIMENTAL RESULTS

Single-crystal $Bi_2Sr_2CaCu_2O_{8+\delta}$,$(Bi-2212)$ was grown at University of Tokyo by using the floating zone technique and post annealed to a slightly over-doped oxygen content ($T_c\simeq 85$ K).[16] Columnar defects with a diameter of about 10

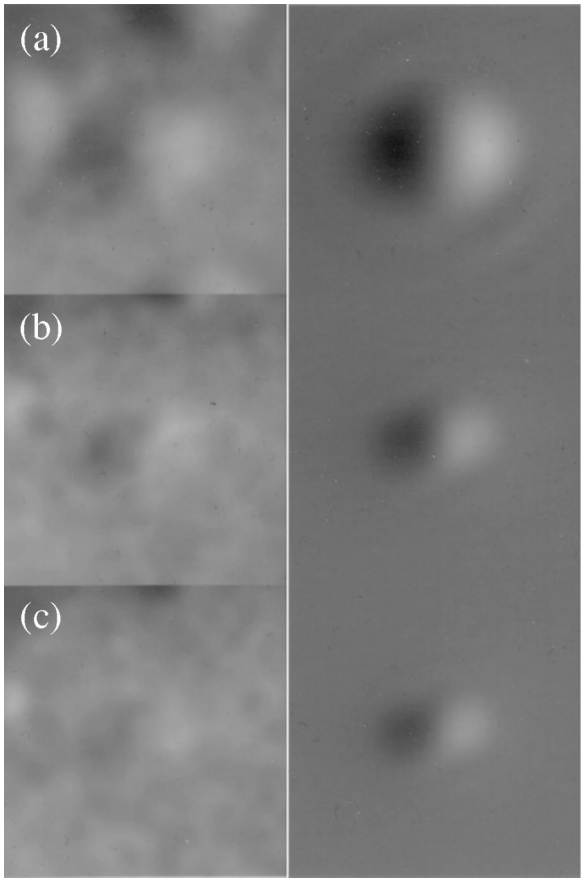


FIG. 11. Out-of-focus images, $\theta=65°, \beta=270°$.

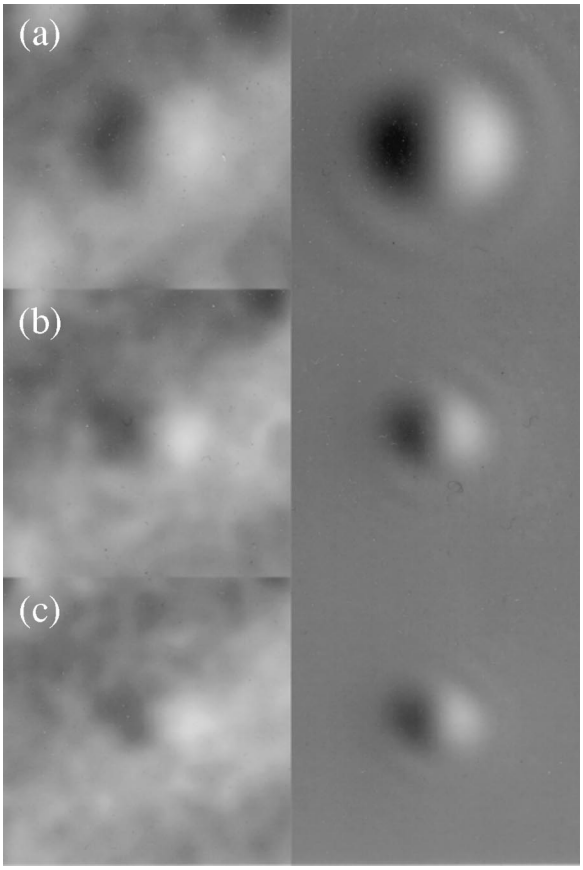


FIG. 12. Out-of-focus images, $\theta=65°, \beta=225°$.

nm were obliquely produced at $\theta=65°$ by irradiation of 240-MeV $Au^{15+}$ ions by using the Tandem Accelerator at the Japan Atomic Energy Research Institute (JAERI).[17] The specimen, observed in the new high voltage holography electron microscope, was cooled to 30 K within the magnetic field at 0.5 mT in order to avoid the effect of intrinsic pinning at lower temperature.[6] The magnetic field, generated by the coils of the special magnetic stage, was always kept oriented parallel to the columnar defects direction.

The Bi-2212 superconductor is characterized by an anisotropy parameter $\gamma$ of the order of 200. In this condition, as explained in Sec. IV, it turns out to be impossible to discriminate between a three dimensional anisotropic structure and a layered one, because of the almost negligible value of the current density along the $c$ axis of the material. Therefore, in the following, only the continuous anisotropic model (which is convenient from the computational point of view, and does not require approximations such as the limit in the number of layers) will be employed in the image interpretation.

The images in the whole residual figures are presented in the following scheme: from top to bottom images corresponding to the three values of the defocus parameter: (a) $Z=1300$ mm, (b) $Z=530$ mm, and (c) $Z=420$ nm are displayed; then, to the left the experimental images and to the right the simulated ones.

In Fig. 8, the case of the unpinned vortex is reported for reference. In this case, the azimuth angle $\beta$ is not significant, as the projection of the vortex core on the object plane is independent of the specimen rotation. The simulations are in good agreement with the experimental results, especially considering that the apparent lower contrast of the micrograph can be explained by the fact that the theoretical simulations do not take into account the effects of partial lateral coherence and inelastic scattering.

Then, the image features corresponding to different azimuth angles can be analyzed, in order to check if we can discriminate between pinned and unpinned vortices. Moreover, we can also have some hints on the sensitivity of the out-of-focus technique over the vortex orientation.

Figures 9, 10, 11, and 12 show out-of-focus images taken at the three different values of defocus at the same specimen region, for different azimuth angles $\beta$ ($\beta=360°$, $\beta=315°$, $\beta=270°$, and $\beta=225°$, respectively) and for a columnar defect tilt $\theta=65°$.

At the highest defocus value of 1300 mm, row (a), all the vortices have a similar appearance of bright-dark globules, i.e., the line dividing the bright and dark regions is roughly aligned along the perpendicular to the tilt axis. This result is agreement with former simulations,[8] showing that at a sufficiently large defocus any kinds of vortices have similar contrast shape independent of their structure. However, it can be noticed that the contrast is slightly different.

By decreasing defocus to 530 mm, row (b), changes in contrast and shape can be seen in the image. This difference is more evident at the small defocus of 420 mm, row (c) (in particular in Fig. 10), where the contrast of vortices becomes

very weak and the vortex shapes are elongated.

In spite of the low contrast value, image noise, and low sensitivity of the phase contrast technique employed, it is possible to distinguish between pinned and unpinned vortices, especially when the experimental conditions are accurately calibrated in order to have the maximum of information. In particular, the specimen should be rotated around its normal **n** in such a way to have the projected core aligned along the tilt axis *y*, and the defocus value should be kept as small as possible, compatible with a sufficient contrast, in order to have the maximum sensitivity on the azimuth angle.

## VII. CONCLUSIONS

It has been shown in this work how the Fourier space approach can be usefully applied for the calculation of the phase shift of superconducting vortices observed by phase contrast electron microscopy techniques.

By this new approach it is possible to evaluate the phase shift in all those cases where the corresponding problem for the magnetic fields can been solved by Fourier methods. In particular, we have been able to obtain in this work the phase shift for a London vortex in an anisotropic thin film, a problem which could only be approximately treated in the previous real space approach.

With this new model, and the recent one of a stack of pancake vortices, we have been able to interpret the main features of the experimental data, obtained with the new high-voltage field-emission electron microscope.

The agreement between experimental data and theoretical interpretation, while demonstrating the ability to distinguish between pinned and unpinned vortices, a result beyond the performance of previous generation instruments, confirms the crucial role played by the anisotropy of the specimen (both in the continuous and layered approaches) in influencing the shape and the contrast of the phase-contrast images obtained by means of the Fresnel out-of-focus method.

## ACKNOWLEDGMENTS

The authors are grateful to Professor J. Shimoyama, Professor T. Hanaguri, Professor K. Kishio, and Professor K. Kitazawa of University of Tokyo for providing Bi-2212 specimen and Dr. S. Okayasu and Dr. M. Sasase of Japan Atomic Energy Research Institute for inducing columnar defects in the specimen. Thanks are also due to T. Akashi of Hitachi Instruments Service Co., Ltd. and S. Saitou, S. Matsunami and N. Moriya of Hitachi, Ltd., for their technical assistance of the experiment and S. Patuelli, Department of Physics, University of Bologna for assistance in preparing the figures.

*Present address: Materials Science Department, Brookhaven National Laboratory, Upton, NY 11973.

†Present address: Central Research Laboratory, Hitachi, Ltd., Kokubunji, Tokyo 185-8601, Japan.

[1] M. Beleggia and G. Pozzi, Ultramicroscopy **84**, 171 (2000).

[2] M. Beleggia and G. Pozzi, Phys. Rev. B **63**, 054507 (2001).

[3] R. Patti and G. Pozzi, Ultramicroscopy **77**, 163 (1999).

[4] J. Pearl, Appl. Phys. Lett. **5**, 65 (1964).

[5] R.G. Mints, V.G. Kogan, and J.R. Clem, Phys. Rev. B **61**, 1623 (2000).

[6] A. Tonomura, H. Kasai, O. Kamimura, T. Matsuda, K. Harada, Y. Nakayama, J. Shimoyama, K. Kishio, T. Hanaguri, K. Kitazawa, M. Sasase, and S. Okayasu, Nature (London) **412**, 620 (2001).

[7] O. Kamimura, H. Kasai, T. Akashi, T. Matsuda, K. Harada, J. Masuko, T. Yoshida, N. Osakabe, A. Tonomura, M. Beleggia, G. Pozzi, J. Shimoyama, K. Kishio, T. Hanaguri, K. Kitazawa, M. Sasase, and S. Okayasu, J. Phys. Soc. Jpn. **71**, 1840 (2002).

[8] S. Fanesi, G. Pozzi, J.E. Bonevich, O. Kamimura, H. Kasai, K. Harada, T. Matsuda, and A. Tonomura, Phys. Rev. B **59**, 1426 (1999).

[9] A. Fukuhara, K. Shinagawa, A. Tonomura, and H. Fujiwara, Phys. Rev. B **27**, 1839 (1983).

[10] G. Pozzi, Adv. Imaging Electron Phys. **93**, 173 (1995).

[11] J.E. Bonevich, K. Harada, H. Kasai, T. Matsuda, T. Yoshida, G. Pozzi, and A. Tonomura, Phys. Rev. B **49**, 6800 (1994).

[12] V.G. Kogan, A.Yu. Simonov, and M. Ledvij, Phys. Rev. B **48**, 392 (1993).

[13] A. Tonomura, *Electron Holography* (Springer, Berlin, 1993).

[14] MATHEMATICA 4.1, Wolfram Research Inc., Champaign, IL, 2000.

[15] T. Pe, M. Benkraouda, and J.R. Clem, Phys. Rev. B **55**, 6636 (1997).

[16] J. Shimoyama, K. Kishio, H. Ikuta, S. Watauchi, M. Okuya, and K. Kitazawa, Physica C **282-287**, 2055 (1997).

[17] S. Okayasu, Y. Kazumata, I. Tanaka, and H. Kojima, Physica B **194-196**, 1881 (1994).